Sensitivity analysis to unsteady perturbations of complex flows: a discrete approach

Oliver M. F. Browne*,†, Gonzalo Rubio, Esteban Ferrer*,† and Eusebio Valero

ETSIA-UPM (School of Aeronautics), Universidad Politecnica de Madrid, Pza. de Cardenal Cisneros 3, 28040 Madrid, Spain

SUMMARY

A discrete framework for computing the global stability and sensitivity analysis to external perturbations for any set of partial differential equations is presented. In particular, a complex-step approximation is used to achieve near analytical accuracy for the evaluation of the Jacobian matrix. Sensitivity maps for the sensitivity to base flow modifications and to a steady force are computed to identify regions of the flow field where an input could have a stabilising effect. Four test cases are presented: (1) an analytical test case to prove the theory of the discrete framework, (2) a lid-driven cavity at low Reynolds case to show the improved accuracy in the calculation of the eigenvalues when using the complex-step approximation, (3) the 2D flow past a circular cylinder at just below the critical Reynolds number used to validate the methodology, and finally, (4) the flow past an open cavity presented to give an example of the discrete method applied to a convectively unstable case. The latter three (2–4) of the aforementioned cases were solved with the 2D compressible Navier–Stokes equations using a Discontinuous Galerkin Spectral Element Method. Good agreement was obtained for the validation test case, (3), with appropriate results in the literature. Furthermore, it is shown that for the calculation of the direct and adjoint eigenmodes and their sensitivity maps to external perturbations, the use of complex variables is paramount for obtaining an accurate prediction.

1. INTRODUCTION

The dynamics of complex aerodynamic flows such as shear layers, cavities, wakes or detached flows present unstable behaviours when some physical dependent parameter (e.g. Reynolds or Mach number) surpasses a critical threshold. In these cases, unstable modes appear and their temporal evolution drives the system dynamics to a new equilibrium configuration, sometimes called the saturated regime. Linear stability analysis studies the appearance and evolution of these modes that are related to parameters involved in the problem [1–3]. Although several examples of stability analysis for different flows can be found in the literature, and are very well documented [4–9], the prediction of the onset of unsteadiness or the characterization of unstable structures in complex 3D geometries or at high Reynolds numbers is still an open problem.

---

*Correspondence to: Oliver M. F. Browne and Esteban Ferrer, ETSIA-UPM (School of Aeronautics), Universidad Politecnica de Madrid, Pza. de Cardenal Cisneros 3, 28040 Madrid, Spain.
†E-mail: oliver.browne@upm.es; esteban.ferrer@upm.es

Recent studies [10, 11] are oriented towards the investigation of the sensitivity of the unstable eigenmodes (i.e. growth rates and frequencies) to the introduction of perturbations in the base flow or to external forces. The pioneering work of Strykowski and Sreenivasan [12] showed, experimentally, that introducing a small object in the wake of a cylinder may delay the onset of unsteadiness, well above the critical Reynolds, for the first bifurcation of Hopf type (at $Re_{\mathrm{crit}} \approx 47$) [13, 14]. In a more general framework, the introduction of a small perturbation in the flow (sucking or blowing, changes to the equilibrium condition or introducing a small control object that acts as a steady force) can have a stabilising or destabilising effect [15]. Sensitivity analysis identifies the regions of the flow where introducing such a modification has the greatest effect on the stability of the flow. This could be of importance to suppress laminar-turbulent transition, to enhance mixing (e.g. vortex generator on a wing to keep boundary layer attached), to prevent the flow from detaching or even to provide means for acoustic control [16, 17].

The numerical study of flow sensitivity relies on the use of adjoint eigenmodes [18, 19]. These modes, which are eigensolutions of an adjoint system of equations, provide receptivity information to external forcing [19, 20]. Sensitivity maps are provided by combining direct and adjoint modes. The importance of adjoint modes and sensitivity maps, together with the mathematical machinery required for the study of the sensitive flow regions to different parameters, has been studied by different authors [8, 18–21]. In addition, these studies provide detailed reviews of the 'state-of-the-art' techniques in linear stability analysis and sensitivity analysis, addressing the relevance that the adjoint plays in the analysis of these problems, and also giving a comprehensive overview of the aforementioned techniques and outlining the possibilities of linking sensitivity information with open/closed loop control.

More precisely, the mathematical formulation and the numerical computation of sensitivities has been detailed by Giannetti and Luchini [10], who showed that the structural sensitivity or 'wave-maker' region may be obtained by combining (using a particular norm) the direct and adjoint eigenmodes. More recently, Marquet *et al.* [22] formulated a method using a continuous approach and Lagrange multipliers to obtain equations for the sensitivity fields for the incompressible Navier–Stokes (NS) equations. In the continuous approach, the adjoint equations are derived from the direct equations (i.e. continuous in space), which are then linearised. Subsequently, the continuous direct and adjoint operators may be formed, and finally, these continuous operators are discretised. Furthermore, Meliga, Sipp and Chomaz [23] computed, also using the continuous framework, the sensitivity to base flow modifications for axisymmetric flows in the compressible regime (subsonic). Meliga *et al.* [24] also employ sensitivity analysis to identify the regions sensitive to a steady force with the aim of using a small control cylinder to alter the shedding frequency aft a D-shaped cylinder geometry.

An alternative is provided by the discrete approach, which is the focus of this paper. The discrete approach requires first the numerical discretisation of the direct equations, which are subsequently linearised to form the direct discrete operator. Chandler *et al.* [21] compared the discrete and the continuous approach for the low Mach number equations for a low-density jet and showed that both methods provide very similar results. On the one hand, the continuous approach, for this particular case, showed a faster rate of convergence while requiring a less resolved mesh. On the other hand, the discrete approach was found to be more straightforward to implement. Mettot *et al.* [25], independently of the authors of this paper, developed a method using a discrete framework to compute the sensitivity to base flow modifications and to steady forcing for high Reynolds number flows with turbulence models using a second-order method for computing the Jacobian and the sensitivity matrix. Additionally, they use finite volumes to discretise their governing equations. They further apply this methodology for finding the regions to place a small control cylinder for stabilising the flow past a D-shaped cylinder in [26]. We hereby extend the methodology of [25, 26] by using a first-order complex-step approximation for the Jacobian and first order for the computation of the sensitivity matrix. It will be shown that the method of the complex-step approximation is advantageous in that it will obtain a higher degree of accuracy (near analytical) with a lower cost of computational time.

In this paper, a methodology to perform global stability and sensitivity analysis using a fully discrete approach is presented. To the authors' knowledge, this is the first such paper to compute the Jacobian using complex variables for a fluid dynamics problem. Furthermore, this is the first sensitivity analysis study to use a high-order spectral element method for the numerics. This study is limited to modal analysis. Non-modal analysis [20], although undoubtedly important, is not within the scope of this work. The discrete approach can be implemented into any kind of computational fluid dynamics (CFD) solver, e.g. laminar or turbulent, or compressible or incompressible. It allows for computing the direct and adjoint modes of the flow, either stable or not, and the sensitivity formulation to these modes. Henceforth, this paper extends the discrete approaches of [21, 25, 26] while also closely following the mathematical formulation of the continuous approach of [22] to retrieve the sensitivity fields for a steady force and to base flow modifications.

The rest of the paper is organized as follows: Section 2 provides the mathematical formulation of the discrete approach; certain details about the application of complex algebra to the computation of function derivatives are included. Section 3 gives a description of the algorithms employed and details their practical implementation. In Section 4, various test cases are included: an analytical test case, lid-driven cavity, circular cylinder and an open cavity. The paper finalises with the conclusions in Section 5.

2. MATHEMATICAL FORMULATION

In what follows, we consider a discretisation of a system of partial differential equations (PDE), typically NS equations, in a computational mesh defined over the problem geometry. The method is independent of the particular numerical scheme used to discretise the spatial derivatives of the equations. However, in this paper, a Discontinuous Galerkin Spectral Element method has been used (see details in Section 3.2). We consider the time varying system

$$\frac{d\mathbf{q}}{dt} = \mathbf{F}(\mathbf{q}), \tag{1}$$

where $\mathbf{q}$ is a vector of dimension N (N = no. of grid points × no. of equations), which contains the number of degrees of freedom for the problem, and $\mathbf{F}(\mathbf{q})$ is a vector of dimension N that defines the numerical fluxes obtained by the discretisation of the continuous PDE in the computational mesh.

Linear stability analysis is charged with determining whether a small disturbance on some base state (the base flow $\bar{\mathbf{q}}$) will become unstable. Hence, the flow is decomposed into a base flow (base state) plus an infinitesimal perturbation (disturbance) such that $\mathbf{q} = \bar{\mathbf{q}} + \mathbf{q}'$. Inserting this decomposition into Equation (1) and then taking Taylor series about the base flow for the numerical fluxes and neglecting second-order $(\mathbf{q}')^2$ terms gives

$$\frac{d\mathbf{q}'}{dt} = \left.\frac{\partial \mathbf{F}(\mathbf{q})}{\partial \mathbf{q}}\right|_{\bar{\mathbf{q}}} \mathbf{q}'. \tag{2}$$

It is assumed that a base flow or steady solution ($\bar{\mathbf{q}}$) that fulfils $\mathbf{F}(\bar{\mathbf{q}}) = \mathbf{0}$ can be computed.

Now, we consider these perturbations in the form of normal modes $\mathbf{q}' = \hat{\mathbf{q}}e^{\sigma t}$, which, when inserted into Equation (2), yields the following eigenvalue problem:

$$\sigma \hat{\mathbf{q}} = \left.\frac{\partial \mathbf{F}(\mathbf{q})}{\partial \mathbf{q}}\right|_{\bar{\mathbf{q}}} \hat{\mathbf{q}} = \mathbf{J}(\bar{\mathbf{q}})\hat{\mathbf{q}}, \tag{3}$$

where $\mathbf{J}(\bar{\mathbf{q}}) = \left.\frac{\partial \mathbf{F}(\mathbf{q})}{\partial \mathbf{q}}\right|_{\bar{\mathbf{q}}}$ is herein referred to as the Jacobian matrix and $\hat{\mathbf{q}}$ is the direct eigenmode of the complex eigenvalue, $\sigma = \sigma_r + \sigma_i$.

In this work, the Jacobian matrix is obtained following a discrete approach: the NS equations are first discretised, Equation (1), and then linearised around a base flow, Equation (2). This approach does not require the implementation of a new solver specifically written for the linear Navier–Stokes equations, and any existing NS solver may be used for computation. However, the detailed
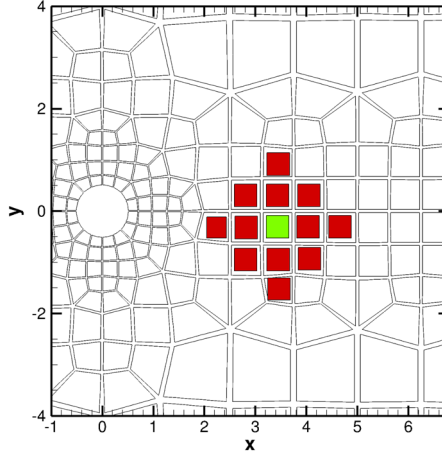
Figure 1. Figure showing an example of the compact stencil used in Jacobian computation. The green square indicates where the perturbation is applied, and the red squares indicate the elements to which the information travels.

implementation of the Jacobian from the numerical scheme may be difficult. A practical alternative is to obtain the Jacobian by numerically differentiating the numerical fluxes around the base flow by using a finite difference approximation. Indeed, using Taylor series,

$$\mathbf{F}(\bar{\mathbf{q}} + \epsilon\mathbf{k}) = \mathbf{F}(\bar{\mathbf{q}}) + \epsilon \left.\frac{\partial\mathbf{F}(\bar{\mathbf{q}})}{\partial\mathbf{q}}\right|_{\bar{\mathbf{q}}} \mathbf{k} + \mathcal{O}(\epsilon^2), \tag{4}$$

where $\mathbf{k}$ is a numerical disturbance (no physical relevance) used to evaluate the Jacobian and ϵ is a relatively small number. Neglecting order ϵ^2 terms and rearranging gives

$$\frac{\mathbf{F}(\bar{\mathbf{q}} + \epsilon\mathbf{k}) - \mathbf{F}(\bar{\mathbf{q}})}{\epsilon} = \left.\frac{\partial\mathbf{F}(\bar{\mathbf{q}})}{\partial\mathbf{q}}\right|_{\bar{\mathbf{q}}} \mathbf{k} \approx \mathbf{J}(\bar{\mathbf{q}})\mathbf{k}. \tag{5}$$

From a practical implementation point of view, to calculate the jth column of the Jacobian, the jth row of the $\mathbf{k}$ vector is set to 1, while the other rows are set to 0. This process is successively repeated for as many number of degrees of freedom of the matrix. The first-order formula, Equation (5), requires the computation of N numerical fluxes, with N being the dimension of $\bar{\mathbf{q}}$. In compact schemes, the perturbation introduced in an element will only affect a limited number of elements (perturbation stencil). In order to reduce the computational cost, only the fluxes in the elements that are part of the stencil need be evaluated. An example of the stencil is given in Figure 1. The numerical evaluation of the Jacobian is well established and is commonly used within the linear stability CFD community [25, 27, 28], to name a few.

In addition, higher-order difference schemes for computing the Jacobian can improve the accuracy of the numerical Jacobian: these schemes have small numerical errors and can be easily implemented but at the expense of additional computation of fluxes [29]. An alternative to improve the accuracy of the Jacobian without sacrificing the computational cost is to use complex variables.

2.1. Complex-step derivative

The method for computing the Jacobian, Equation (5), is a forward first-order finite difference approximation. To obtain accurate results, one needs to choose a value for the increment ϵ that is small enough such that the truncation error is not significant while remaining not too small to keep round-off errors controlled when subtracting numbers that are almost equal.

An efficient way to overcome these difficulties is to use complex variables for the computations. The complex-step derivative approximation can be used to determine first derivatives providing near analytic accuracy. Early work on obtaining derivatives via a complex-step approximation in order to improve overall accuracy can be found in [30, 31].

The advantages of the complex-step derivative approach over a standard finite difference include the following: (1) the Jacobian approximation is not subject to subtractive cancellations inherent to round-off errors, (2) it can be used on discontinuous functions and (3) it is easy to implement in a black-box manner, thereby making it applicable to general non-linear functions.

The derivation of the complex-step derivative approximation is accomplished by approximating a non-linear function with a complex variable using a Taylor series expansion:

$$f(x + i\epsilon) = f(x) + \frac{df}{dx}i\epsilon - \frac{d^2 f}{dx^2}\frac{\epsilon^2}{2} - \mathcal{O}(i\epsilon^3 + \epsilon^4), \tag{6}$$

taking the imaginary part of each term and neglecting higher-order ϵ^2 terms, we obtain the approximation

$$\frac{df}{dx} = \frac{Im[f(x + i\epsilon)]}{\epsilon} + \mathcal{O}(\epsilon^2), \tag{7}$$

where Im denotes the imaginary part.

Additional information can be found in [32], which shows that not only a wider range of step sizes can be selected for the complex approach, but a higher level of precision can be achieved (near to machine precision). On the downside, the use of this approach means that it is necessary to implement a complex version of the NS fluxes. However, modern computer languages (e.g. FORTRAN 90, C++, etc) enable the ease of implementation of these changes through function overloading or template techniques.

2.2. Adjoint operator

The corresponding discrete adjoint matrix can also be calculated. First, an inner product for a pair of continuous vectors, $\tilde{\mathbf{c}}$ and $\tilde{\mathbf{d}}$, is defined as

$$\langle\tilde{\mathbf{c}}, \tilde{\mathbf{d}}\rangle = \int_\Omega \tilde{\mathbf{c}}^*\tilde{\mathbf{d}}\, d\Omega = \mathbf{c}^*\mathbf{M}\mathbf{d}, \tag{8}$$

where $*$ denotes the conjugate transpose, $\mathbf{c}$ and $\mathbf{d}$ are the discretised version of $\tilde{\mathbf{c}}$ and $\tilde{\mathbf{d}}$ in the computational domain, Ω, and $\mathbf{M}$ is the mass matrix associated to a spatial discretisation selected for the discrete approach. For example, in our high-order Discontinuous Galerkin (DG) solver, the mass matrix is diagonal (see Section 3.2).

A matrix, $\mathbf{A}$, and its discrete adjoint, $\mathbf{A}^+$, can be related in the following expression:

$$\langle\mathbf{A}\tilde{\mathbf{c}}, \tilde{\mathbf{d}}\rangle = \langle\tilde{\mathbf{c}}, \mathbf{A}^+\tilde{\mathbf{d}}\rangle. \tag{9}$$

Considering the definition of an inner product defined in Equation (8), we obtain

$$\begin{aligned} (\mathbf{A}\mathbf{c})^*\mathbf{M}\mathbf{d} &= \mathbf{c}^*\mathbf{M}\mathbf{A}^+\mathbf{d}, \\ \mathbf{c}^*\mathbf{A}^*\mathbf{M}\mathbf{d} &= \mathbf{c}^*\mathbf{M}\mathbf{A}^+\mathbf{d}, \\ \mathbf{A}^*\mathbf{M} &= \mathbf{M}\mathbf{A}^+, \\ \mathbf{M}^{-1}\mathbf{A}^*\mathbf{M} &= \mathbf{A}^+, \end{aligned} \tag{10}$$

an expression that relates the conjugate transpose of the Jacobian to its adjoint.

Therefore, the standard direct and adjoint eigenvalue problems are given by

$$\mathbf{J}(\bar{\mathbf{q}})\hat{\mathbf{q}} = \sigma\hat{\mathbf{q}}, \tag{11}$$

$$\mathbf{J}^+(\bar{\mathbf{q}})\hat{\mathbf{q}}^+ = \sigma^*\hat{\mathbf{q}}^+, \tag{12}$$

where according to the definition of the adjoint Equation (10), $\mathbf{J}^+(\bar{\mathbf{q}})$ is the adjoint of the Jacobian and $\hat{\mathbf{q}}^+$ is the adjoint eigenmode.

2.3. Sensitivity maps

The interest for sensitivity analysis is how an eigenvalue will change, if at all, with some arbitrary modification to the flow. In this work, we consider the sensitivity of the eigenvalue subject to a modification of the base flow, $\delta\bar{\mathbf{q}}$, or steady forcing, $\delta\mathbf{q_f}$. If $\Delta\sigma$ is defined as the variation of the eigenvalue subjected to external perturbations, the following relation holds [22]

$$\Delta_{\bar{\mathbf{q}}}\sigma = \langle\nabla_{\bar{\mathbf{q}}}\sigma, \delta\bar{\mathbf{q}}\rangle, \tag{13}$$

$$\Delta_{\mathbf{qf}}\sigma = \langle\nabla_{\mathbf{qf}}\sigma, \delta\mathbf{q_f}\rangle. \tag{14}$$

The resulting sensitivity fields $\nabla_{\bar{\mathbf{q}}}\sigma, \nabla_{\mathbf{qf}}\sigma$, can be obtained following the method of Lagrangian multipliers [20], which is aimed at maximising the change in the variable, σ, subject to some constraints. This approach is described by Marquet *et al.* [22] to derive the equations for the sensitivity fields in a continuous approach. Here, we extend this analysis to a discrete approach. The mathematical formulation details are given in Appendix A, and only the final results are summarised here:

$$\nabla_{\bar{\mathbf{q}}}\sigma = \mathbf{B}^+(\bar{\mathbf{q}}, \hat{\mathbf{q}})\hat{\mathbf{q}}^+, \tag{15}$$

$$\nabla_{\mathbf{qf}}\sigma = \bar{\mathbf{q}}^+ = (\mathbf{J}^+(\bar{\mathbf{q}}))^{-1}\mathbf{B}^+(\bar{\mathbf{q}}, \hat{\mathbf{q}})\hat{\mathbf{q}}^+ = (\mathbf{J}^+(\bar{\mathbf{q}}))^{-1}\nabla_{\bar{\mathbf{q}}}\sigma. \tag{16}$$

Here, $\bar{\mathbf{q}}^+$ is the adjoint of the base flow, obtained from the solutions of Equation (16), and $\mathbf{B}(\bar{\mathbf{q}}, \hat{\mathbf{q}})$ is the sensitivity matrix, obtained through differentiating the Jacobian and direct mode corresponding to the most unstable eigenvalue with respect to the base flow:

$$\mathbf{B}(\bar{\mathbf{q}}, \hat{\mathbf{q}}) = \frac{\partial(\mathbf{J}(\bar{\mathbf{q}})\hat{\mathbf{q}})}{\partial\bar{\mathbf{q}}}. \tag{17}$$

Additionally, a normalization condition for the eigenmode $\hat{\mathbf{q}}$ and its adjoint $\hat{\mathbf{q}}^+$ is obtained:

$$\langle\hat{\mathbf{q}}^+, \hat{\mathbf{q}}\rangle = 1. \tag{18}$$

3. ALGORITHMS

The procedure for performing sensitivity analysis, when using a discrete approach, is summarised here:

1. Calculate the base flow by solving a steady solution of system of PDEs, Equation (1).
2. Compute the Jacobian matrix using complex variables, Equation (7).
3. Compute the adjoint matrix, Equation (10).
4. Solve the direct and adjoint eigenvalue problems, Equations (11) and (12).
5. Normalize adjoint modes, Equation (18).
6. Compute the sensitivity matrix, Equation (17), and multiply with leading adjoint mode to get sensitivity to base flow modifications, Equation (15).
7. Solve the system, Equation (16), to obtain the sensitivity to a steady force.

3.1. Implementation details

In order to implement the previous algorithms, a NS solver with the capability to compute the fluxes using complex variables is necessary. Following Equation (7), the jth column of the Jacobian matrix is obtained by computing

$$\frac{Im(\mathbf{F}(\bar{\mathbf{q}} + i\epsilon\mathbf{k}))}{\epsilon} = \mathbf{J}(\bar{\mathbf{q}})\mathbf{k}, \qquad (19)$$

where the vector $\mathbf{k}$ is set to 1 in the jth row and to 0 in the other entries. The previous formula includes an error of $\mathcal{O}(\epsilon^2)$, and so it is expected that for $\epsilon \approx 10^{-7}$, machine precision is obtained in the computation of the Jacobian.

Following each computation of the jth column of the Jacobian matrix, only the non-zero values that are part of the stencil are stored in the aptly named compressed sparse column format. With this format, the matrix now comprises three vectors: a vector containing the cumulative number of non-zeros per column that has a dimension equal to that of $N + 1$, a vector containing the row index for each of the non-zero values that intuitively has a dimension equal to the number of non-zeros and a vector containing the non-zero values of the Jacobian that again has the dimension equal to the number of non-zeros of the problem. The number of non-zeros will depend on the number nodes in the mesh, the number of equations being solved and the size of the stencil that is computed for the jth column of the Jacobian matrix. For example, the number of degrees of freedom (N) for the case of flow around a circular cylinder, described in Section 4.3, is equal to 64 000, which, if formed explicitly in double precision, would require almost 31 GB of memory ($64\,000^2$). By using the compressed sparse column format, the number of non-zeros reduces to 41 million, which corresponds to a total memory, for all three vectors, of 0.61 GB.

It is evident that the number of non-zeros per row (note: the aforementioned vector contains the number of non-zeros per column) for the Jacobian matrix is equal to the number of non-zeros per column for the adjoint matrix. Thus, a simple algorithm is used to transpose the Jacobian to form the adjoint matrix without explicitly forming the adjoint.

The computation of the sensitivity matrix, $\mathbf{B}(\bar{\mathbf{q}}, \hat{\mathbf{q}})$, is performed in the following way, since, the only resource available is the NS fluxes $\mathbf{F}$. Moreover, we have to keep in mind that an explicit version of the Jacobian is not known, only its numerical values. From its definition, it follows that $\mathbf{B}(\bar{\mathbf{q}}, \hat{\mathbf{q}})$ is a linear function of $\hat{\mathbf{q}} = \hat{\mathbf{q}}_\mathbf{R} + i\hat{\mathbf{q}}_\mathbf{I}$ and a non-linear function of $\bar{\mathbf{q}}$ through the Jacobian of $\mathbf{F}$. Thus,

$$\mathbf{B}(\bar{\mathbf{q}}, \hat{\mathbf{q}}) = \frac{\partial(\mathbf{J}(\bar{\mathbf{q}})\hat{\mathbf{q}})}{\partial\bar{\mathbf{q}}} \qquad (20)$$

can be decomposed into its real and imaginary parts:

$$\mathbf{B}(\bar{\mathbf{q}}, \hat{\mathbf{q}}) = \mathbf{B}_R(\bar{\mathbf{q}}, \hat{\mathbf{q}}) + i\,\mathbf{B}_I(\bar{\mathbf{q}}, \hat{\mathbf{q}}) = \frac{\partial(\mathbf{J}(\bar{\mathbf{q}})\hat{\mathbf{q}}_R)}{\partial\bar{\mathbf{q}}} + i\,\frac{\partial(\mathbf{J}(\bar{\mathbf{q}})\hat{\mathbf{q}}_I)}{\partial\bar{\mathbf{q}}}. \qquad (21)$$

Additionally,

$$\mathbf{J}(\bar{\mathbf{q}})\hat{\mathbf{q}} = \left.\frac{\partial\mathbf{F}(\bar{\mathbf{q}})}{\partial\mathbf{q}}\right|_{\bar{\mathbf{q}}} \hat{\mathbf{q}} \qquad (22)$$

(for either the real or imaginary part of $\hat{\mathbf{q}}$) is simply the directional derivative of $\mathbf{F}(\bar{\mathbf{q}})$ along $\hat{\mathbf{q}}$; thus,

$$\mathbf{J}(\bar{\mathbf{q}})\hat{\mathbf{q}} = \frac{\mathbf{F}(\bar{\mathbf{q}} + \epsilon_1\hat{\mathbf{q}}) - \mathbf{F}(\bar{\mathbf{q}})}{\epsilon_1} + \mathcal{O}(\epsilon_1). \qquad (23)$$

Therefore, neglecting order ϵ_1 terms,

$$\frac{\partial(\mathbf{J}(\bar{\mathbf{q}})\hat{\mathbf{q}})}{\partial\bar{\mathbf{q}}} = \frac{1}{\epsilon_1}\left(\left.\frac{\partial\mathbf{F}(\bar{\mathbf{q}})}{\partial\mathbf{q}}\right|_{\bar{\mathbf{q}}+\epsilon_1\hat{\mathbf{q}}} - \left.\frac{\partial\mathbf{F}(\bar{\mathbf{q}})}{\partial\mathbf{q}}\right|_{\bar{\mathbf{q}}}\right) = \frac{1}{\epsilon_1}\left(\left.\frac{\partial\mathbf{F}(\bar{\mathbf{q}})}{\partial\mathbf{q}}\right|_{\bar{\mathbf{q}}+\epsilon_1\hat{\mathbf{q}}} - \mathbf{J}(\bar{\mathbf{q}})\right), \qquad (24)$$

where the definition of the Jacobian, Equation (3), has been used. The right-hand side expression can be evaluated using complex variables, thus giving the following expression for the sensitivity matrix:

$$\mathbf{B}(\bar{\mathbf{q}}, \hat{\mathbf{q}}) = \frac{1}{\epsilon_1}\left[\left(\frac{Im(\mathbf{F}(\bar{\mathbf{q}} + \epsilon_1\hat{\mathbf{q}}_\mathbf{R} + i\epsilon\mathbf{k}))}{\epsilon} - \mathbf{J}(\bar{\mathbf{q}})\right) + i\left(\frac{Im(\mathbf{F}(\bar{\mathbf{q}} + \epsilon_1\hat{\mathbf{q}}_\mathbf{I} + i\epsilon\mathbf{k}))}{\epsilon} - \mathbf{J}(\bar{\mathbf{q}})\right)\right].$$
$$(25)$$

In a similar fashion to the computation of the Jacobian in Equation (19), Equation (25) is evaluated by successively computing columns of $\mathbf{B}(\bar{\mathbf{q}}, \hat{\mathbf{q}})$ by setting one row of vector $\mathbf{k}$ to 1 and the rest to 0. In the previous expression, only one column of the Jacobian $\mathbf{J}(\bar{\mathbf{q}})$ is considered at each time, although one can consider computing, in one iteration, all the non-interacting columns. Additionally, the sensitivity matrix, $\mathbf{B}(\bar{\mathbf{q}}, \hat{\mathbf{q}})$, or its conjugate transpose, need never be formed explicitly for the calculation of Equations (15) and (16). From expression (10), it can be seen that Equation (15) can be written explicitly as

$$\nabla_{\bar{\mathbf{q}}}\sigma = \mathbf{M}^{-1}\mathbf{B}^*(\bar{\mathbf{q}}, \hat{\mathbf{q}})\mathbf{M}\hat{\mathbf{q}}^+, \qquad (26)$$

where $\mathbf{B}^*(\bar{\mathbf{q}}, \hat{\mathbf{q}})$ is the conjugate transpose of the sensitivity matrix. It is a trivial task to multiply the mass matrix, $\mathbf{M}$, which, as mentioned in our DG approach, is diagonal, with the adjoint mode $\hat{\mathbf{q}}^+$ to give a new vector $\mathbf{d}$:

$$\nabla_{\bar{\mathbf{q}}}\sigma = \mathbf{M}^{-1}\mathbf{B}^*(\bar{\mathbf{q}}, \hat{\mathbf{q}})\mathbf{d}. \qquad (27)$$

Thus, by setting the first row of the $\mathbf{k}$ vector equal to 1 and the rest 0, we obtain the first column of the sensitivity matrix, $\mathbf{B}(\bar{\mathbf{q}}, \hat{\mathbf{q}})$. If we take the complex conjugate of this vector, we will get the first row of the transpose of the sensitivity matrix, $\mathbf{B}^*(\bar{\mathbf{q}}, \hat{\mathbf{q}})$. By multiplying this row vector now with the vector $\mathbf{d}$, we obtain a scalar value. We proceed to multiply this with the first row of the inverse of the mass matrix, $\mathbf{M}^{-1}$, which returns the first row of the sensitivity to base flow modifications vector, $\nabla_{\bar{\mathbf{q}}}\sigma$.

The previous algorithm obtains first-order accuracy in ϵ_1 and second-order accuracy in ϵ and requires three computations of the fluxes per grid node. Second-order precision in ϵ can be easily obtained by using a central difference scheme in Equation (23) but at the additional cost of a new evaluation of the fluxes.

In Section 4, expressions (19) and (25) are first checked against a simple analytical test and then applied to the lid-driven cavity flow, to the solution aft a circular cylinder and to an open cavity flow.

3.2. High-order Navier–Stokes solver

The computationally demanding nature of the NS solution, in the stability analysis context, leads to the selection of high-order numerical schemes for the numerical discretisation of system Equation (28). High-order methods (spectral type methods) have been extensively used in CFD due to their accuracy and efficiency in the simulation of fluid flows. In particular, these methods are suitable for problems where high accuracy is required and, hence, are well suited to track the evolution of small perturbations as in stability analysis.

The numerical scheme used in this work discretises the compressible NS equations following a Discontinuous Galerkin Spectral Element Method (DGSEM [33]) for the spatial operators, coupled with a time integration scheme of order 3. The DGSEM is a nodal collocation form of the discontinuous Galerkin method where the solution is approximated by a tensor product of Lagrange polynomials and where inner products are evaluated using Gauss-Legendre quadrature [33, 34].

A summary of the mathematical formulation of the DGSEM is now presented. The general 3D formulation is detailed hereafter, but the test cases considered in this paper, which employ the DGSEM method, are strictly 2D.

The NS equations constitute a system of PDEs that can be shortly written in vector form as

$$\frac{\partial \mathbf{q}}{\partial t} + \nabla \cdot \mathbf{F}(\mathbf{q}) = \mathbf{0}, \tag{28}$$

where $\mathbf{q}$ represents the vector of conservative variables and $\mathbf{F}(\mathbf{q})$ represents the 3D fluxes, including convective and diffusive in the three coordinate directions.

To solve our set of equations in general 2D or 3D geometries, the original domain is divided into non-overlapping hexahedral sub-domains, E_{sd}, such that $\Omega = \sum_{\text{sd}} E_{\text{sd}}$. Inside each sub-domain, a polynomial of degree, P, is used to approximate the unknowns and the fluxes, $\mathbf{q}, \mathbf{F}$; thus,

$$\mathbf{q}^P = \sum_{i,j,k=0}^{P} \mathbf{q}_{i,j,k} \Phi_{i,j,k}, \quad \mathbf{F}^P = \sum_{i,j,k=0}^{P} \mathbf{F}(\mathbf{q}_{i,j,k}) \Phi_{i,j,k}, \tag{29}$$

where

$$\Phi_{i,j,k} = L_i(x) L_j(y) L_k(z)$$

is the tensor product of the Lagrange interpolant in the nodes i, j, k and $\mathbf{q}_{i,j,k}$ is the value of the unknown in each computational node. In this work, the nodes in each direction follow a Gauss-Legendre distribution, and the basis functions $L_{(i,j,k)}$ are taken as the Lagrange interpolant at these nodes.

Reconsidering Equation (28), we obtain, at an element level, the following discretised equation:

$$\frac{\partial \mathbf{q}^P}{\partial t} + \nabla \cdot \mathbf{F}^P = 0. \tag{30}$$

DGSEM makes use of the Garlekin weak form of the equations and a discontinuous treatment of the interfaces and boundaries. Thus, Equation (30) is multiplied by a test function (the same function as the basis for the Galerkin method) and integrated in the computational space, then the error is forced to be orthogonal at each test function $\Phi_{i,j,k}$ in a mesh element E_{sd}, yielding

$$\left(\frac{\partial \mathbf{q}^P}{\partial t}, \Phi_{i,j,k} \right)_{E_{\text{sd}}} + (\nabla \cdot \mathbf{F}^P, \Phi_{i,j,k})_{E_{\text{sd}}} = 0, \quad (i,j,k) = 0, \dots, P,$$

with $(a,b)_{E_{\text{sd}}} = \int_{E_{\text{sd}}} ab \, d\Omega$, defining an inner product (typically the L_2 inner product). After integrating by parts, we obtain

$$\left(\frac{\partial \mathbf{q}^P}{\partial t}, \Phi_{i,j,k} \right)_{E_{\text{sd}}} - (\nabla \Phi_{i,j,k}, \cdot \mathbf{F}^P)_{E_k} + \int_{\partial E_{\text{sd}}} \Phi_{i,j,k} \mathbf{F}^P \cdot \mathbf{n} \vec{d}S = 0, \tag{31}$$

where the third term (the surface integral) extends over the boundary ∂E_{sd} of the computational element E_{sd}, with external pointing normal $\mathbf{n}$. This boundary may lie at the interface between two elements or at physical boundary conditions, and in both cases, the treatment is similar. Note that all integrals in Equation (31) can be numerically evaluated using Gauss quadrature.

To obtain a solution over the complete discretised computational domain ($\Omega = \sum_{\text{sd}} E_{\text{sd}}$), it is necessary to sum all the element contributions:

$$\left(\frac{\partial \mathbf{q}^P}{\partial t}, \Phi_{i,j,k} \right)_{\Omega} - (\nabla \Phi_{i,j,k}, \cdot \mathbf{F}^P)_{\Omega} + \sum_{\gamma \in \Gamma} \int_{\gamma} \Phi_{i,j,k} \mathbf{F}^*(\mathbf{n}, \mathbf{q}^L, \mathbf{q}^R) \vec{d}S = 0, \tag{32}$$

where Γ denotes the set of internal edges in the mesh Ω. In addition, note that we have replaced $\mathbf{F}^P$ with $\mathbf{F}^*(\mathbf{n}, \mathbf{q}^L, \mathbf{q}^R)$ in the surface integral. $\mathbf{F}^*(\mathbf{n}, \mathbf{q}^L, \mathbf{q}^R)$ represents the numerical flux between two consecutive elements in the mesh (*L*eft and *R*ight). These numerical fluxes arise from the discontinuous Galerkin setting, where we consider that each element is disconnected from the next and hence contains a complete set of degrees of freedom to represent a polynomial of order P.

Taking into account the decomposition of the unknown in Equation (29) and the orthogonality of the Lagrange basis in the Gauss nodes, the following expression is finally obtained for the integrals of Equation (32):

$$\frac{\partial \mathbf{q}_{i,j,k}}{\partial t} + \mathcal{D}_x \mathbf{F}^1_{i,j,k} + \mathcal{D}_y \mathbf{F}^2_{i,j,k} + \mathcal{D}_z \mathbf{F}^3_{i,j,k} = 0, \quad (i, j, k) = 0, \dots, P. \tag{33}$$

The discrete divergence (second term of the previous equation) is obtained after the numerical integration of the second and third terms of Equation (32). Gauss quadrature is used to evaluate these integrals, giving

$$\mathcal{D}_x \mathbf{F}^1_{i,j,k} = \mathbf{F}^{1*}(x, y_j, z_k) \left. \frac{L_i(x)}{w_i} \right|_{x=0}^{x=1} - \sum_{m=0}^{P} \mathbf{F}^1_{m,j,k} d_{i,m}$$

$$\mathcal{D}_y \mathbf{F}^2_{i,j,k} = \mathbf{F}^{2*}(x_i, y, z_k) \left. \frac{L_j(y)}{w_j} \right|_{y=0}^{y=1} - \sum_{m=0}^{P} \mathbf{F}^2_{i,m,k} d_{j,m} \tag{34}$$

$$\mathcal{D}_z \mathbf{F}^3_{i,j,k} = \mathbf{F}^{3*}(x_i, y_j, z) \left. \frac{L_k(z)}{w_k} \right|_{z=0}^{z=1} - \sum_{m=0}^{P} \mathbf{F}^3_{i,j,m} d_{k,m}, \quad \text{with} \quad d_{m,n} = \frac{L'_m(s_n) w_n}{w_m}.$$

In the previous expression, w_n are the Gauss integration weights in direction $n = x$, y or z; $L'_m(s_n)$ is the derivative of the Lagrange interpolant evaluate in the node s_n, and $\mathbf{F}^*$ are the interface fluxes. These fluxes can be differentiated into viscous or inviscid. Computation of inviscid fluxes requires taking into account the left and right values of the unknowns at each interface. Let us note that taking the average value of the unknowns $\mathbf{q}$ at the interface (equivalent to a central scheme) provides a numerically unstable scheme when the convective terms dominate and is only recommended at very low Reynolds numbers. For larger *Re*, an up-winding scheme should be used instead. The most common way to introduce up-winding in the scheme is by solving the equivalent Riemann problem at the interface. In the particular case of Euler equations (or inviscid NS), a different Riemann solver has been already developed. In this work, a Roe Riemann solver has been used in the computations [35].

The viscous fluxes require discretisations for elliptic type equations. A simple approach consists of averaging the right and left viscous fluxes at the interface, but this solution has been proved numerically unstable for implicit schemes. A more general framework for derivation and analysis of discontinuous Galerkin methods for elliptic equations (e.g. interior penalty, Local Discontinuous Galerkin, Bassi-Rebay) was derived in [36]. Additional information of this methodology can be found in [33]. In our explicit time marching method, we use the Bassi-Rebay approach to calculate the diffusive fluxes.

Once the numerical fluxes and associated Jacobian are obtained, the eigenvalues and eigenvectors are computed using a shift and invert methodology to obtain the most unstable eigenvalue. This methodology requires the computation of a lower upper (LU) factorisation of the Jacobian matrix $\mathbf{J}(\bar{\mathbf{q}})$, which is performed using the libraries for sparse matrices of MUMPS [37]. Subsequently, the Arnoldi iteration is employed; a direct solver of MUMPS is used to build each column of the Krylov subspace, and LAPACK [38] is used to recover the eigenvalues and corresponding eigenvectors. The influence of the dimension of Krylov subspace used in the Arnoldi methods was assessed and finally set to 1000 in all cases. Using this dimension for the Krylov subspace, no variations in the magnitude of the most unstable eigenvalues were observed. Additionally, the computation of the sensitivity to a steady force requires the solution of Equation (16), which is performed using the current LU

factorisation of $\mathbf{J}(\bar{\mathbf{q}})$ previously obtained with MUMPS. In this work, we have used MUMPS in parallel. This entails writing an algorithm that splits the matrix onto each local processor. For larger problems, where LU factorisation and direct solvers are impractical, the Krylov iterative methods generalized minimal residual method (GMRES) and preconditioners (incomplete LU factorisation) may be more appropriate, although this extension is not considered here.

4. TEST CASES

To prove the theory of the discrete framework and to show the accuracy of the methodology, a simple problem with analytical solution is presented. Subsequently, the lid-driven cavity problem is presented for validation purposes. This applies the methodology to the compressible Navier–Stokes equations but for a case where the dimension of the Jacobian is relatively small to compare the difference in eigenvalues when using (19) and (25). The NS flow aft a circular cylinder at Reynolds number 45 and Mach number (Ma) of 0.2 is presented to give an example of a globally unstable case. These results are compared with those of other authors [10, 22] to further validate the methodology and implementation. Finally, the flow past an open cavity is provided to give an example of a convectively unstable case.

4.1. Analytical test case

Let us define the flux vector as

$$\mathbf{F}(\bar{\mathbf{q}}) = \begin{bmatrix} \bar{u}\bar{v} \\ \bar{u}\bar{w}^3 \\ \bar{v}\bar{w} \end{bmatrix}, \tag{35}$$

where

$$\bar{\mathbf{q}} = (\bar{u}, \bar{v}, \bar{w})^T. \tag{36}$$

It may be easily checked that the analytical Jacobian and sensitivity matrices are given by the following:

$$\mathbf{J}(\bar{\mathbf{q}}) = \begin{bmatrix} \bar{v} & \bar{u} & 0 \\ \bar{w}^3 & 0 & 3\bar{u}\bar{w}^2 \\ 0 & \bar{w} & \bar{v} \end{bmatrix}, \qquad \mathbf{B}(\bar{\mathbf{q}}, \hat{\mathbf{q}}) = \begin{bmatrix} \hat{q}_2 & \hat{q}_1 & 0 \\ 3\bar{w}^2\hat{q}_3 & 0 & 3\bar{w}^2\hat{q}_1 + 6\bar{u}\bar{w}\hat{q}_3 \\ 0 & \hat{q}_3 & \hat{q}_2 \end{bmatrix}, \tag{37}$$

where

$$\hat{\mathbf{q}} = (\hat{q}_1, \hat{q}_2, \hat{q}_3)^T. \tag{38}$$

The Jacobian and sensitivity matrices are then calculated using the algorithms detailed in the previous section, subject to epsilon, ϵ and ϵ_1, values ranging from 10^5 to 10^{-15}. Results using real and complex variables are compared. The relative error between the numerical and analytical matrices are plotted in Figure 2.

If we arbitrarily take 10^{-5} as the maximum allowable error, which is acceptable, and examine Figure 2, the following observations and conclusions can be drawn:

1. Figure 2(a): Calculating the Jacobian with real variables using a first-order approach restricts the choice of ϵ to a narrow range 10^{-5} to 10^{-11}. Using a second-order central difference approach for the numerical evaluation of the Jacobian enables more flexibility in the choice of epsilon, but a second-order approach is more computationally expensive because it requires the calculation the fluxes twice.
2. Figure 2(b): Calculating the Jacobian with the complex-step approximation gives acceptable results for any value of epsilon smaller than $10^{-2.5}$. Furthermore, error that levels out at machine precision ($\sim 10^{-15}$) can be obtained for $\epsilon = 10^{-7}$.
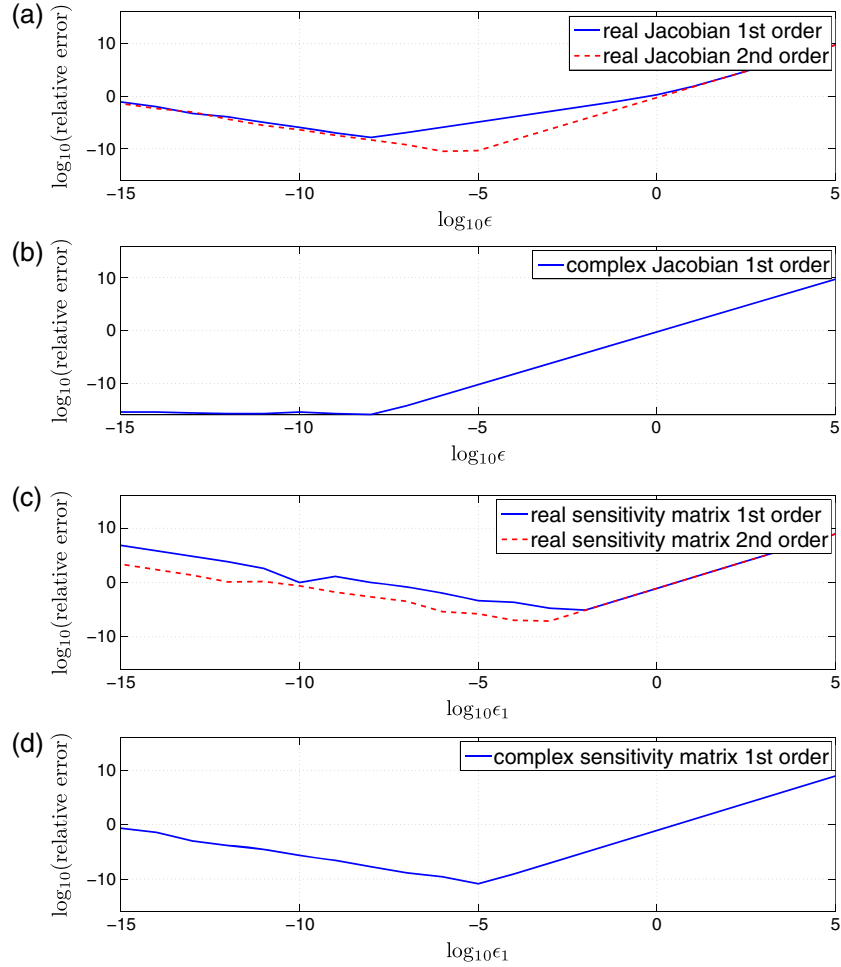
Figure 2. Comparison of numerical and analytical Jacobian, (a) and (b), and sensitivity matrix, (c) and (d), for test case Equation (37) as a function of ϵ, Equation (19), and ϵ_1, Equation (25). The sensitivity matrices computed in (c) and (d) are computed using the ϵ value in the corresponding Jacobian calculation (real or complex) that gives lowest relative error. The sensitivity matrix is calculated using Equation (25).

3. Figure 2(c): Using a first-order method, with real variables and the epsilon value, ϵ, held at its optimal value from Figure 2(a) (10^{-8}), for the calculation of the sensitivity matrix $\mathbf{B}(\bar{\mathbf{q}}, \hat{\mathbf{q}})$ gives an acceptable result only when a value of epsilon, ϵ_1, equal to 10^{-2} is selected. In addition, it can be seen that little improvement on relative error and the range of acceptable epsilon, ϵ_1, values is achieved by moving to a second-order method ($\epsilon = 10^{-8}$).

4. Figure 2(d): A first-order method with the complex-step approximation for the sensitivity matrix enables a greater range of epsilon, ϵ_1, values (10^{-2} to 10^{-10}) with improved accuracy.

It is evident that for the calculation of both the Jacobian and sensitivity matrix that the complex-step approximation method is more robust and more accurate with fewer flux evaluations. This alone warrants the use of this method, but if one wishes to achieve an 'acceptable' solution for the sensitivity matrix, it becomes paramount that the complex-step approximation method is selected.

4.2. Lid-driven cavity: choice for ϵ and ϵ_1

The effect of the choice of epsilon values for the high-order compressible NS solver will now be explored. It was shown in Section 4.1 and in [39] that for $\epsilon >\approx 10^{-7}$ the relative error reduces to machine precision when using the complex-step derivative approximation. The lid-driven cavity is run with the following conditions: $Re = 200$, $Ma = 0.2$, four quadrilateral elements each with
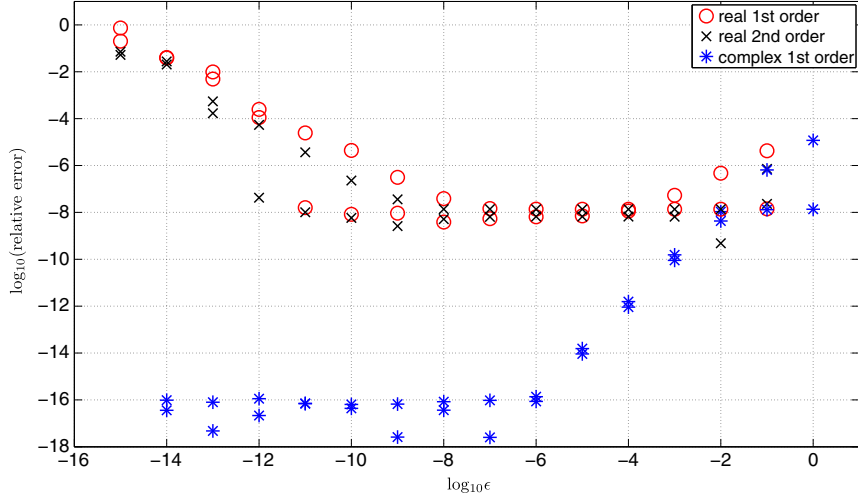
Figure 3. Comparison of first-order, second-order and first-order complex-step approximation methods for the numerical differentiation of the fluxes to calculate the Jacobian. The relative error for the two most unstable eigenvalues are shown for the lid-driven cavity case.

$P = 8$. A base flow is obtained, and then the Jacobian is computed using a first-order method, Equation (5), a second-order method (see [25]), and a complex-step approximation, Equation (7). Figure 3 shows relative error of the two most unstable eigenvalues for the three aforementioned methods with varying epsilon, ϵ. It is assumed that the true values for the eigenvalues are calculated with Equation (7) using $\epsilon = 10^{-15}$, and these are then used as the reference values when calculating the relative error. From Figure 3, it can be seen that the first-order complex-step approximation method converges at $\epsilon = 10^{-6}$ for a relative error of 10^{-16}. Furthermore, both the first-order and second-order methods initially decrease (truncation error is decreasing) to a relative error of $\sim 10^{-8}$ for epsilon, ϵ, ranging from 10^{-4} to 10^{-7}. The relative error begins to increase (round-off error becomes significant) for $\epsilon > 10^{-7}$. Close inspection of ϵ values ranging from 10^{-1} to 10^{-3} reveals that the first-order and second-order methods converge with slopes of 1 and 2, respectively. The complex-step approximation method converges with a gradient of 2, and significantly, but unlike the second-order method, it only requires one evaluation of the fluxes. Furthermore, in our implementation, the cost for one computation is comparable between the real and complex formulations. Indeed, the complex approximation provides greater accuracy whilst having a lower computational cost.

The choice of ϵ_1 is more challenging. Mettot *et al.* [25] present a value of $\epsilon_1 = (5 \times 10^{-6})(|\bar{\mathbf{q}}|+1)$ based on the work of [28, 40]. This value corresponds well with the optimal value for ϵ_1 given for the analytical case in Figure 2(d). There is only a necessity to tune ϵ_1 to reduce the error in Equation (25) because the Jacobian, $\mathbf{J}(\bar{\mathbf{q}})$, is computed to near analytical accuracy. For the rest of this paper, we take $\epsilon = 10^{-10}$ and $\epsilon_1 = (5 \times 10^{-6})(|\bar{\mathbf{q}}| + 1)$.

4.3. Flow around a circular cylinder at $Re = 45$

The flow aft a circular cylinder is studied for $Re = 45$ (below critical Reynolds number). This problem, studied by several authors (see Table I), shows a Hopf bifurcation at the at $Re_{\text{crit}} \approx 47$. Above this, a global instability (Kármán vortex street) develops. We have chosen $Re = 45$ to compare the accuracy of our methodology with other authors' work in the literature [22, 25]. Contrary to other authors [10, 22, 41], the compressible NS are used in this study; therefore, in order to reproduce previous results and for validation purposes, the Mach number is set to 0.2, being a compromise between numerical accuracy and compressible effects.

After a preliminary study for the convergence of the solution (not shown), the final mesh is composed of 640 quadrilateral elements with polynomials of order $P = 4$. As the state vector is composed of four variables, the number of degrees of freedom (N) for the problem is 64 000

Table I. Numerical comparison of the non-dimensional frequency
of the least stable eigenvalue for the circular test case.

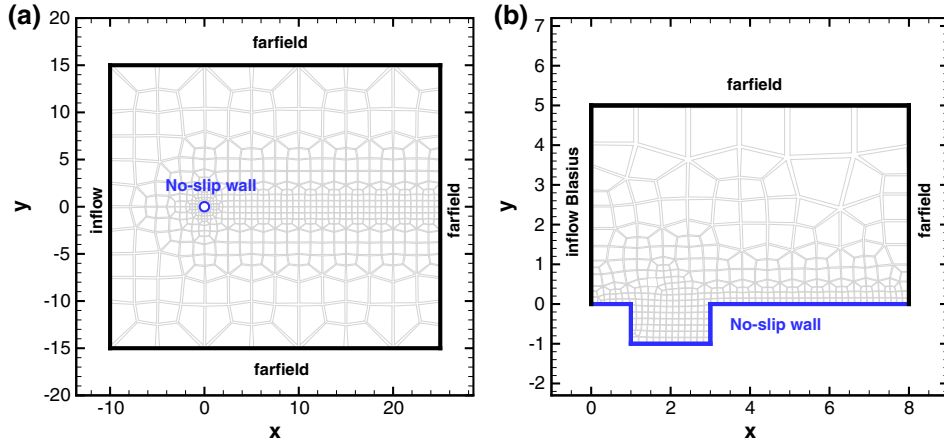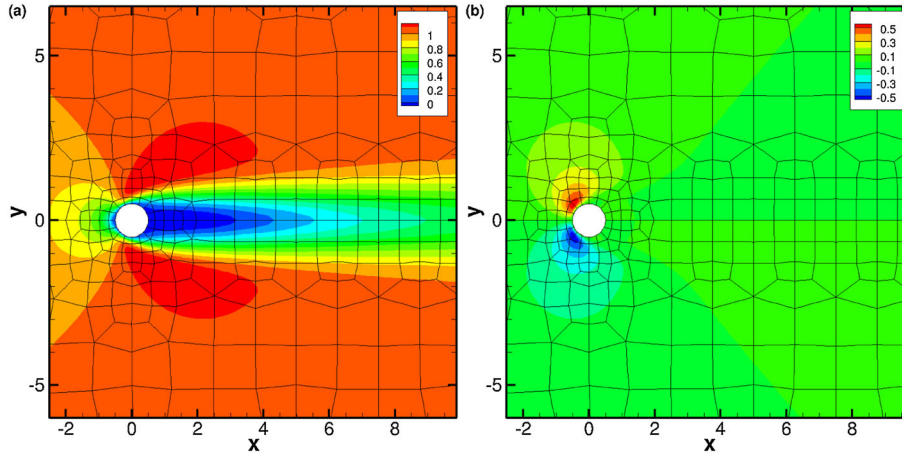|	Frequency $\left(f = \frac{\sigma_i}{2\pi} \right)$
Marquet *et al.* [22] $Re = 46.8$	~ 0.116
Giannetti and Luchini [10] $Re = 45$	~ 0.1177
Ferrer *et al.* [41] $Re = 45$	~ 0.118
Current study $Re = 45$	~ 0.118

Figure 4. Overview of the dimensions and boundary conditions for (a) cylinder and (b) open cavity.

Figure 5. Cylinder base flow fields; (a) $\overline{\rho u}$ and (b) $\overline{\rho v}$.

(No of DoF = 640× (P+1)^2 × No of Equations), where the number of equations is set to 4 (2D NS compressible equations).

The base flow is a steady solution ($\mathbf{F}(\bar{\mathbf{q}}) = 0$) and is computed by time marching the unsteady solver (third-order Runge–Kutta method) until convergence. The computational domain and outline of the boundary conditions is given in Figure 4. Figure 5 shows the base flow fields for $\overline{\rho u}$ and $\overline{\rho v}$. The symmetric and stable recirculation bubble can be seen aft of the cylinder (5(a)). The concentration of elements in the region local to the cylinder is also visible in this figure. For this base flow, the Jacobian and its eigenvalues are computed following the procedures described in previous sections. We are only concerned with the least stable eigenmode (the one that defines the onset of unsteadiness). Finally, the frequency associated to the least stable perturbation is compared in Table I against solutions provided by other authors, validating our methodology and analysis.
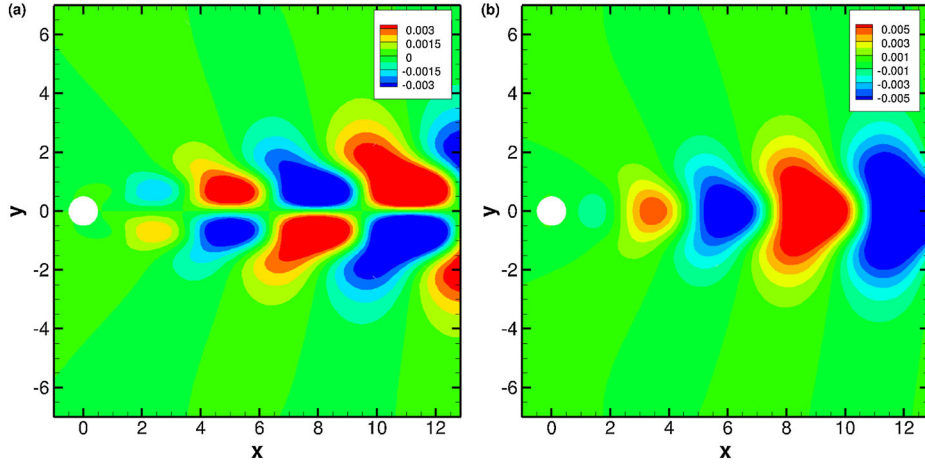
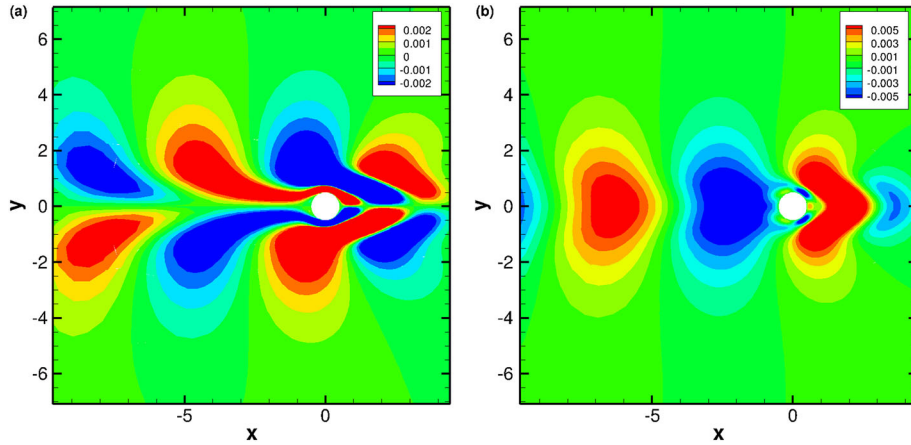Figure 6. The real part of the cylinder direct eigenmode fields; (a) $\widehat{\rho u}$ and (b) $\widehat{\rho v}$.

Figure 7. The real part of the cylinder adjoint eigenmode fields; (a) $\widehat{(\rho u)^+}$ and (b) $\widehat{(\rho v)^+}$.

Figure 6 shows the real part of the direct eigenmodes associated to the least stable eigenvalue for the $\widehat{\rho u}$ (left) and $\widehat{\rho v}$ (right) components of velocity. The $\widehat{\rho u}$ eigenmode is antisymmetric about the centreline ($y = 0$), whereas the $\widehat{\rho v}$ eigenmode is symmetric about the same line. Both show similar structures to that of the Kármán vortex street, which is present at Reynolds numbers close to the critical value.

Similarly, Figure 7 shows the real part of the adjoint velocities, $\widehat{(\rho u)^+}$ (left) and $\widehat{(\rho v)^+}$ (right). As expected, but contrariwise to the direct eigenmode, the structures of interest for the adjoint are located upstream of the cylinder [19]. The structural sensitivity of the flow can be calculated using the dot product of the velocity components of the direct and adjoint eigenmodes ($\|\hat{\mathbf{u}}\|.\|\hat{\mathbf{u}}^+\|$) and is shown in Figure 8. According to these results, the maximum sensitivity region (also called the wavemaker) occurs at the centre of the two distorted ovals at ($x = 2.5$ and $y = \pm 0.5$), namely the region of flow where small modifications produce the larger variations in the eigenvalues. Despite the use of the compressible NS equations, a quantitative and qualitative agreement is obtained with the results of other authors [10, 22, 41]. The boundary conditions for the adjoint matrix are automatically applied in the discrete framework when solving the system, Equation (12), as stated by [10]. Furthermore, it is also clear from Figure 8 that the wavemaker is far enough from the inlet and farfield boundaries and therefore the influence of boundary conditions is minimised for this absolutely unstable flow case.
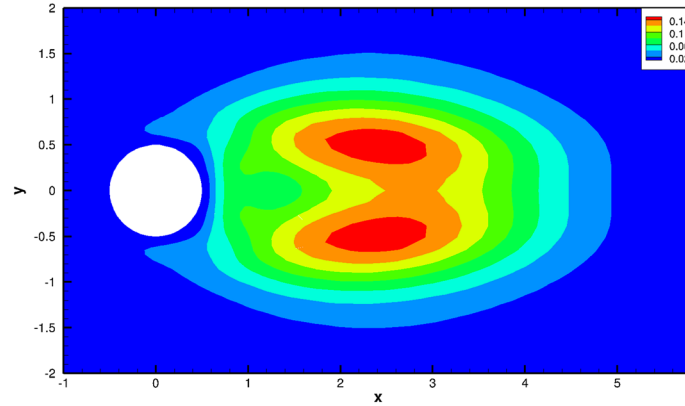
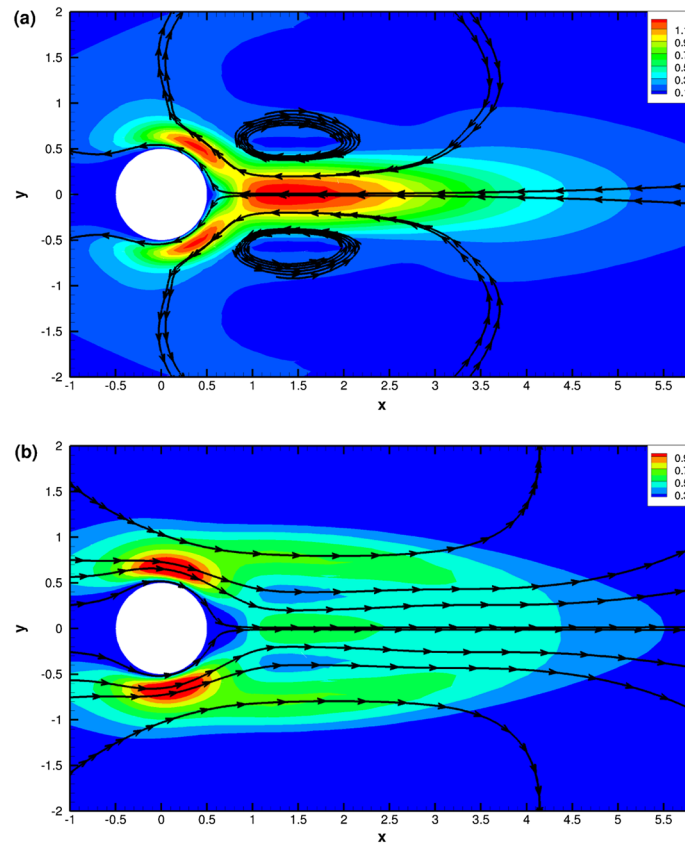Figure 8. Structural sensitivity $\|\hat{\mathbf{u}}\|.\|\hat{\mathbf{u}}^+\|$ for the circular cylinder at $Re = 45$.

Figure 9. Sensitivity to a steady force; (a) real part, $\nabla_{\mathbf{qf}}\sigma_r$, and (b) imaginary part, $\nabla_{\mathbf{qf}}\sigma_i$, for the circular cylinder part.

Finally, Figure 9 shows the real (upper) and imaginary (lower) part of the sensitivity to a steady force, $\nabla_{\mathbf{qf}}\sigma$. The results are in excellent agreement with the sensitivity maps published by Marquet *et al.* [22]. Three main regions are identified where the flow is most sensitive: (1) one diameter to two diameters downstream of the cylinder along $y = 0$, (2) very close (downstream) the cylinder at plus 45° from $y = 0$ and (3) very close (downstream) the cylinder at −45° from $y = 0$.

Moreover, Figure 9 gives us the regions of the flow where inputting a steady force would have the greatest effect or, to be more specific, the greatest drift in eigenvalue and, hence, stabilise or destabilise the flow. By examining Figure 9(a), it can be delineated that inputting a steady force at

$(x = 1, y = 0)$ and orientated upstream (opposite direction to the flow) would decrease the growth rate, σ_r, and subsequently stabilise the flow. It can be seen in Figure 9(b) that the same force would result in an increase in the frequency, σ_i.

4.4. Open cavity flow at $Re = 1400$

To further validate the method, a convectively unstable case is presented. For a system to be convectively unstable, the instabilities must grow in space but not in time. The open cavity is chosen to demonstrate the methodology in the context of a convectively unstable flow. The open cavity flow shows a global instability inside the cavity, while a convective instability develops upstream of the cavity. The discretised computational domain can be seen in Figure 4 with the corresponding boundary conditions. The inflow boundary condition is computed by solving the Blasisus boundary layer equations based on the Reynolds number, Re, and a desired boundary layer thickness, Θ_{inlet}. The Reynolds number, $Re = \frac{U_\infty D}{\upsilon} = 1400$ (based on the cavity depth, D, free-stream velocity, U_∞, and kinematic viscosity, υ) and dimensionless boundary layer thickness, $\Theta_{\text{inlet}} = \frac{\Theta}{D} = 0.0337$, are both given as a function of the cavity depth, D. The computational mesh comprises 394 quadrilateral elements, each with $P = 4$. The problem has been extensively studied by de Vicente [3] and Mesegur et $al.$ [42], who show that convective stability of the system is strongly dependent on the outflow boundary condition. Their work is used for validating the base flow at $Re = 1400$. The outflow boundary condition does not affect the frequency, σ_i, but can affect the growth rate, σ_r, of the
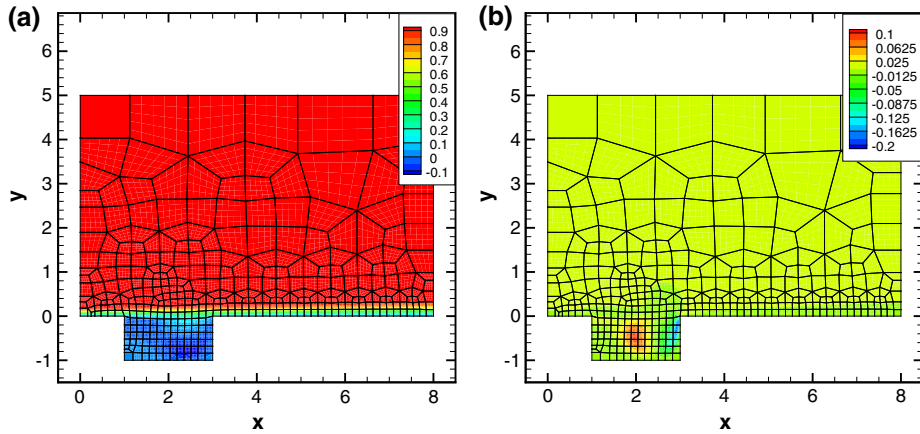

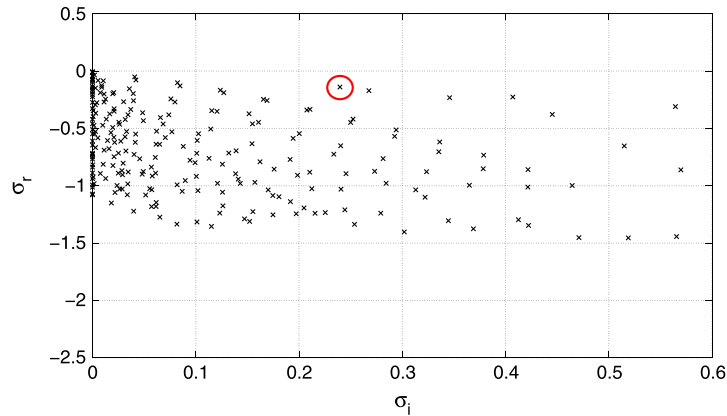Figure 10. Open cavity base flow fields at $Re = 1400$; (a) $\overline{\rho u}$ and (b) $\overline{\rho v}$.

Figure 11. The eigenvalue spectrum for flow past an open cavity at $Re = 1400$. The circled eigenvalue corresponds to the first Rossiter mode.

system because the outflow boundary condition can modify the spatial growth of the disturbance for this convectively unstable case.

The base flow fields, $\overline{\rho u}$ and $\overline{\rho v}$, for the open cavity can be seen in Figure 10. These agree well with other studies in the literature [3, 42].

Figure 11 shows the eigenvalue spectrum computed for the open cavity. The eigenvalue that corresponds to the first Rossiter mode is selected. This corresponds to the eigenvalue that is circled in Figure 11. In this case, this is not the most unstable eigenvalue but it is known from [42–44] that as the Reynolds number increases the growth rate, σ_r, for this eigenvalue will eventually become positive. We achieve a frequency of $f = 0.236$, and Table II compares this result with other studies. It can be seen that relatively good agreement has been achieved. The eigenmodes corresponding to this eigenvalue are shown in Figure 12. A structure similar to a Tollmien–Schlichting wave, present in boundary layer flows, can be seen for both $\widehat{\rho u}$ and $\widehat{\rho v}$. The adjoint modes can be seen in Figure 13.

Table II. Numerical comparison of the non-dimensional frequency of the least stable eigenvalue for the flow past an open cavity.

	Frequency $\left(f = \frac{\sigma_i}{2\pi} \right)$
Messeguar *et al.* [42]	~ 0.25
Rowley *et al.* [43]	~ 0.26
Current study	~ 0.24

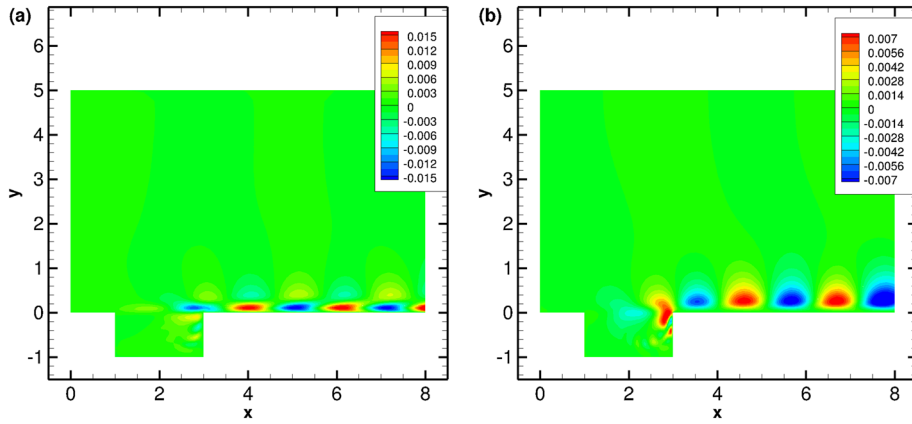Figure 12. The real part of the open cavity direct eigenmode fields; (a) $\widehat{\rho u}$ and (b) $\widehat{\rho v}$.
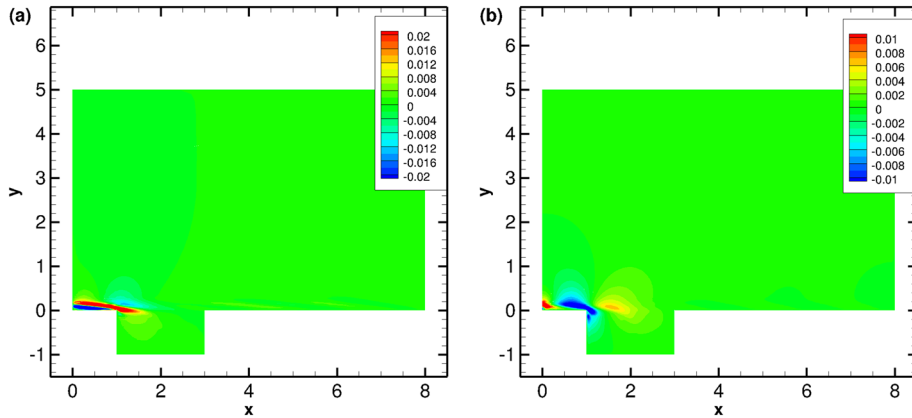

Figure 13. The real part of the open cavity adjoint eigenmode fields; (a) $\widehat{(\rho u)}^+$ and b) $\widehat{(\rho v)}^+$.
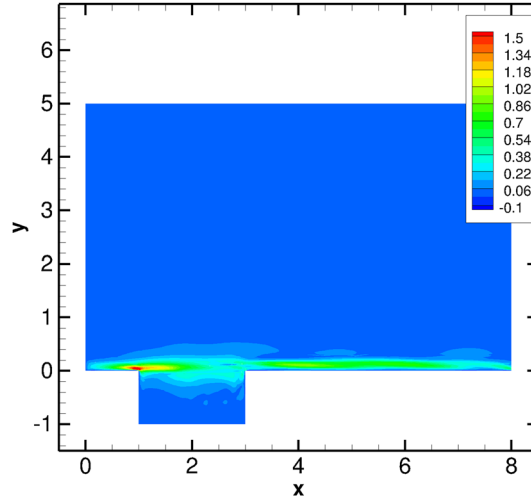
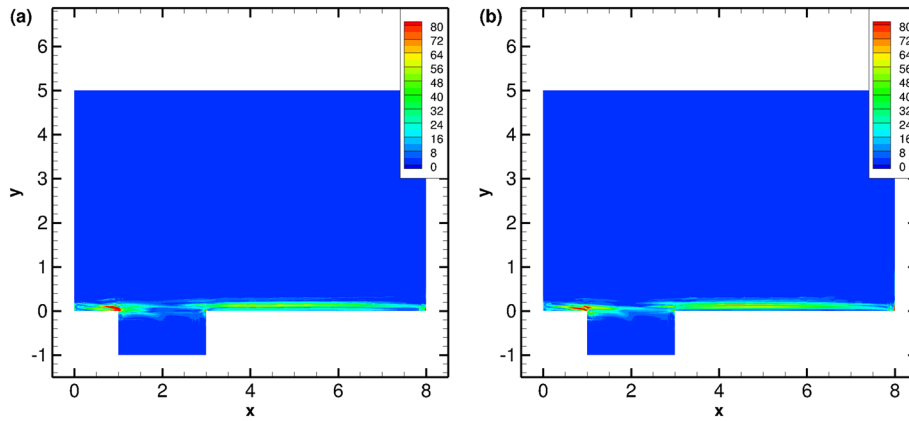Figure 14. Structural sensitivity $\|\hat{\mathbf{u}}\|.\|\hat{\mathbf{u}}^+\|$ for the open cavity at $Re = 1400$.

Figure 15. Sensitivity to base flow modifications, (a) $\nabla_{\bar{\mathbf{q}}}\sigma_r$ and (b) $\nabla_{\bar{\mathbf{q}}}\sigma_i$, for the open cavity at $Re = 1400$.
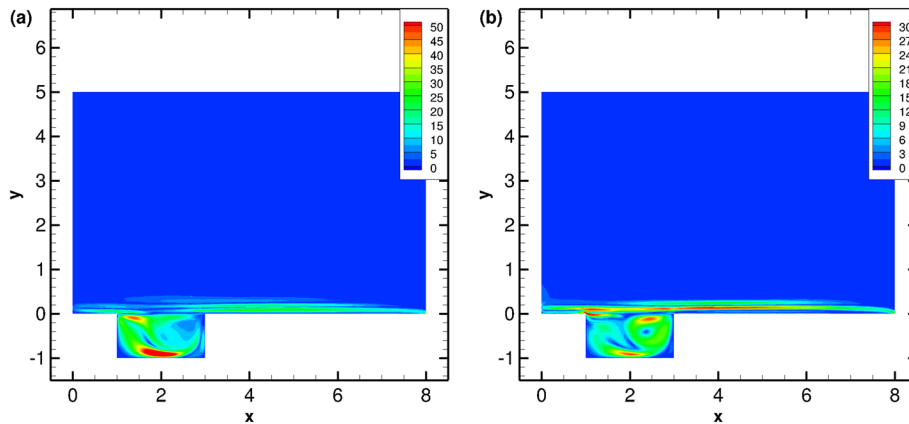

Figure 16. Sensitivity to a steady force, (a) real part, $\nabla_{\mathbf{qf}}\sigma_r$, and (b) imaginary part, $\nabla_{\mathbf{qf}}\sigma_i$, for the open cavity at $Re = 1400$.

These modes give information about the most receptive regions, and, as would be expected, these are found just upstream of the cavity.

Figure 14 shows the structural sensitivity for flow past an open cavity. It can be seen that the 'wavemaker' region is located just upstream of the leading edge of the cavity. This is the region just before the boundary layer detaches, so it is intuitive that this would be the wavemaker. Figure 15 shows the sensitivity of the open cavity to the base flow modifications, $\nabla_{\bar{q}}\sigma$. It can be seen that for both the growth rate, $\nabla_{\bar{q}}\sigma_r$, and the frequency, $\nabla_{\bar{q}}\sigma_i$, the region of the flow that is most sensitive is located just upstream of the cavity. This indicates here that a base flow perturbation could have a stabilising effect on the wave that can be seen in Figure 12 for $\widehat{\rho u}$ and $\widehat{\rho v}$. Figure 16 shows the sensitivity to a steady force, $\nabla_{\mathbf{q_f}}\sigma$. Contrariwise to Figure 15, Figure 16 indicates that putting a steady force inside the cavity will have the greatest stabilising effect. There is also a region downstream of the leading edge of the cavity where a force could also be put to have the same effect.

5. CONCLUSION

This paper has presented a general numerical methodology for conducting sensitivity and stability analysis. Although the method could be applied to any PDE containing a spatial operator and a time derivative, in this paper, it has been investigated for the compressible NS equations. It was found that it is insufficient to use a standard finite difference approximation to obtain an accurate sensitivity matrix when analysing a small problem with an analytical solution. To overcome this problem, the method of complex-step approximation has been used and has shown to provide a far superior prediction of the sensitivity matrix at a reduced computational cost. It was also shown for the lid-driven cavity case that near analytic accuracy can be achieved for Jacobian calculation when using complex variables. The method has been validated using the flow past a circular cylinder at a Reynolds number below critical Reynolds number. Good quantitative and qualitative agreement has been found with published data for the same test case, where the continuous approach was used together with the incompressible NS equations. The sensitivity maps correctly show the regions of the flow that are most sensitive when subjected to a steady force. Flow past an open cavity was also presented to give an example of a convectively unstable case. The proposed method also agrees well in the prediction of the eigenvalues with other authors for this case. The discrete approach offers advantages over the continuous approach:

1. The adjoint base flow equations do not need to be computed. This is the case for the continuous approach, but this is achieved for the discrete approach with Equation (10).
2. If a continuous approach was opted for, then to compute the sensitivity to a steady force, the NS equations (condensed form of Equation (1)) would need to be recomputed but with an extra source term, $\nabla_{\bar{q}}\sigma$, inserted.
3. Near to analytic accuracy is achieved for the Jacobian matrix when employing complex variables.

The application of this methodology to more complex models, including turbulence models and highly compressible flows, is straightforward and may give valuable information of the regions of the flow where the applications of a small perturbation can produce the maximum output.

APPENDIX A: DERIVATION OF SENSITIVITY FIELDS

A.1 Sensitivity to a steady force

The discrete mathematical formulation of the sensitivity of a given eigenvalue (eigenmode) to the introduction of a steady force in the flow is derived herein.

From the steady solution of Equation (1), we consider a forcing term $\mathbf{q_f}$,

$$\mathbf{F}(\bar{\mathbf{q}}) = \mathbf{q_f}, \tag{A.1}$$

and would like to obtain information about the flow field, where a perturbation would give the greatest drift in the eigenvalues. Thus, it makes sense to use the method of Lagrangian multipliers, where we maximise the change in the eigenvalue, $\Delta\sigma$, subject to some physical constraints. The Lagrangian functional reads

$$L(\bar{\mathbf{q}}, \sigma, \hat{\mathbf{q}}, \mathbf{q_f}, \bar{\mathbf{q}}^+, \hat{\mathbf{q}}^+) = \sigma + \langle \hat{\mathbf{q}}^+, \mathbf{J}(\bar{\mathbf{q}})\hat{\mathbf{q}} - \sigma\hat{\mathbf{q}} \rangle - \langle \bar{\mathbf{q}}^+, \mathbf{F}(\bar{\mathbf{q}}) - \mathbf{q_f} \rangle, \tag{A.2}$$

where the complex Lagrangian multipliers, $\hat{\mathbf{q}}^+$ and $\bar{\mathbf{q}}^+$, are the adjoint eigenmodes and adjoint base flow, respectively. The constraints are the direct eigenvalue problem, Equation (11), and the steady NS equations with a forcing term, Equation (A.1). Equation (A.2) is differentiated with respect to the state variable, $(\bar{\mathbf{q}}, \sigma, \hat{\mathbf{q}})$. The derivative with respect to the adjoint variables provides the initial eigenvalue and the NS equations. Derivation with respect to $(\bar{\mathbf{q}}, \sigma, \hat{\mathbf{q}})$ gives

$$\frac{\partial L}{\partial \hat{\mathbf{q}}}\delta\hat{\mathbf{q}} = \langle \hat{\mathbf{q}}^+, (\mathbf{J}(\bar{\mathbf{q}}) - \sigma\mathbf{I})\delta\hat{\mathbf{q}} \rangle = 0, \tag{A.3}$$

$$= \langle (\mathbf{J}(\bar{\mathbf{q}}) - \sigma\mathbf{I})^+\hat{\mathbf{q}}^+, \delta\hat{\mathbf{q}} \rangle = 0, \tag{A.4}$$

$$\mathbf{J}^+(\bar{\mathbf{q}})\hat{\mathbf{q}}^+ = \sigma\hat{\mathbf{q}}^+, \tag{A.5}$$

$$\frac{\partial L}{\partial \sigma}\delta\sigma = \delta\sigma + \langle \hat{\mathbf{q}}^+, -\delta\sigma\mathbf{I}\hat{\mathbf{q}} \rangle = 0, \tag{A.6}$$

$$= \delta\sigma - \delta\sigma\langle \hat{\mathbf{q}}^+, \mathbf{I}\hat{\mathbf{q}} \rangle = 0, \tag{A.7}$$

$$\langle \hat{\mathbf{q}}^+, \hat{\mathbf{q}} \rangle = 1, \tag{A.8}$$

$$\frac{\partial L}{\partial \bar{\mathbf{q}}}\delta\bar{\mathbf{q}} = \left\langle \hat{\mathbf{q}}^+, \frac{\partial(\mathbf{J}(\bar{\mathbf{q}})\hat{\mathbf{q}})}{\partial \bar{\mathbf{q}}}\delta\bar{\mathbf{q}} \right\rangle - \langle \bar{\mathbf{q}}^+, \mathbf{J}(\bar{\mathbf{q}})\delta\bar{\mathbf{q}} \rangle = 0, \tag{A.9}$$

$$\langle \mathbf{B}^+(\bar{\mathbf{q}}, \hat{\mathbf{q}})\hat{\mathbf{q}}^+, \delta\bar{\mathbf{q}} \rangle - \langle \mathbf{J}^+(\bar{\mathbf{q}})\bar{\mathbf{q}}^+, \delta\bar{\mathbf{q}} \rangle = 0, \tag{A.10}$$

$$\mathbf{J}^+(\bar{\mathbf{q}})\bar{\mathbf{q}}^+ = \mathbf{B}^+(\bar{\mathbf{q}}, \hat{\mathbf{q}})\hat{\mathbf{q}}^+. \tag{A.11}$$

Three equations are recovered from this method: the adjoint eigenvalue problem, Equation (A.5), a normalization condition, Equation (A.8), and an equation relating the adjoint eigenmode with the adjoint base flow, Equation (A.11).

The gradient of the Lagrangian with respect to a steady force $\mathbf{q_f}$ is

$$\frac{\partial L}{\partial \mathbf{q_f}}\delta\mathbf{q_f} = \langle \bar{\mathbf{q}}^+, \delta\mathbf{q_f} \rangle. \tag{A.12}$$

Assuming that the gradient of the Lagrangian with respect to a steady force and the gradient of σ with respect to a steady force are equal, then the shift in eigenvalue, Equation (14), can be rewritten as

$$\Delta\sigma = \langle \nabla_{\mathbf{q_f}}\sigma, \delta\mathbf{q}_f \rangle = \frac{\partial L}{\partial \mathbf{q_f}}\delta\mathbf{q_f}, \tag{A.13}$$

providing the sensitivity to a steady force as

$$\nabla_{\mathbf{q_f}}\sigma = \bar{\mathbf{q}}^+. \tag{A.14}$$

A.2 Sensitivity to base flow modifications

The Lagrangian functional for sensitivity to base flow modifications is

$$L(\bar{\mathbf{q}}, \sigma, \hat{\mathbf{q}}, \hat{\mathbf{q}}^+) = \sigma + \langle \hat{\mathbf{q}}^+, \mathbf{J}(\bar{\mathbf{q}})\hat{\mathbf{q}} + \sigma\hat{\mathbf{q}}), \bar{\mathbf{q}} \rangle. \tag{A.15}$$

Differentiating the Lagrangian functional with respect to $\bar{\mathbf{q}}$, we obtain

$$\frac{\partial L}{\partial \bar{\mathbf{q}}} \delta \bar{\mathbf{q}} = -\langle \hat{\mathbf{q}}^+, \mathbf{B}(\bar{\mathbf{q}}, \hat{\mathbf{q}})\delta \bar{\mathbf{q}} \rangle, \tag{A.16}$$

$$= \langle \mathbf{B}^+(\bar{\mathbf{q}}, \hat{\mathbf{q}})\hat{\mathbf{q}}^+, \delta \bar{\mathbf{q}} \rangle = \langle \nabla_{\bar{\mathbf{q}}}\sigma, \delta \bar{\mathbf{q}} \rangle. \tag{A.17}$$

Hence, the sensitivity to base flow modifications is

$$\nabla_{\bar{\mathbf{q}}}\sigma = \mathbf{B}^+(\bar{\mathbf{q}}, \hat{\mathbf{q}})\hat{\mathbf{q}}^+. \tag{A.18}$$

REFERENCES

1. Schmid P, Henningson D. *Stability and Transition in Shear Flows*. Springer: Manchester, 2001.
2. Sipp D, Barbagallo A, Marquet O, Meliga P. Dynamics and control of global instabilities in open-flows: a linearized approach. *Applied Mechanics Reviews* 2010; **63**(3).
3. De Vicente J. Spectral multidomain methods for global instability analysis of complex cavity flows. *Ph.D. Thesis*, Universidad Politecnica de Madrid, 2010.
4. Bagheri S, Åkervik E, Brandt L, Henningson DS. Matrix-free methods for the stability and control of boundary layers. *AIAA Journal* 2009; **47**(5):1057–1068.
5. Barkley D. Confined three-dimensional stability analysis of the cylinder wake. *Physics Review E* 2005; **71**(017301).
6. Bres GA, Colonius T. Three-dimensional instabilities in compressible flows over open cavities. *Journal of Fluid Mechanics* 2008; **599**:309–339.
7. de Vicente J, Rodriguez D, Theofilis V, Valero E. Stability analysis in spanwise-periodic double-sided lid-driven cavity flows with complex cross-sectional profiles. *Computers & Fluids* 2011; **43**(1):143–153.
8. Huerre P, Monkewitz PA. Local and global instabilities in spatially developing flows. *Annual Review of Fluid Mechanics* 1990; **22**(1):473–537.
9. Theofilis V. Global linear instability. *Annual Review of Fluid Mechanics* 2011; **43**(1):319–352.
10. Giannetti F, Luchini P. Structural sensitivity of the first instability of the cylinder wake. *Journal of Fluid Mechanics* 2007; **581**:167–197.
11. Luchini P, Giannetti F, Pralits J. Structural sensitivity of the finite-amplitude vortex shedding behind a circular cylinder. In *IUTAM Symposium on Unsteady Separated Flows and their Control*, vol. 14, IUTAM Bookseries. Springer: Netherlands, 2009; 151–160.
12. Strykowski PJ, Sreenivasan KR. On the formation and suppression of vortex at low Reynolds numbers. *Journal of Fluid Mechanics* 1990; **218**:71–107.
13. Barkley D. Linear analysis of the cylinder wake mean flow. *Europhysics Letters* 2006; **75**(5):750–756.
14. Barkley D, Henderson RD. Three-dimensional Floquet stability analysis of the wake of a circular cylinder. *Journal of Fluid Mechanics* 1996; **322**:215–241.
15. Collis SS, Joslin RD, Seifert A, Theofilis V. Issues in active flow control: theory, control, simulation, and experiment. *Progress in Aerospace Sciences* 2004; **40**:237–289.
16. Alizard F, Robinet JC. Modeling of optimal perturbations in flat plate boundary layer using global modes: benefits and limits. *Theoretical and Computational Fluid Dynamics* 2011; **25**(1-4):147–165.
17. Jones LE, Sandberg RD, Sandham ND. Stability and receptivity characteristics of a laminar separation bubble on an aerofoil. *Journal of Fluid Mechanics* 2010; **648**:257–296.
18. Chomaz JM. Global instabilities in spatially developing flows: non-normality and nonlinearity. *Annual Review of Fluid Mechanics* 2005; **37**(1):357–392.
19. Luchini P, Bottaro A. Adjoint equations in stability analysis. *Annual Review of Fluid Mechanics* 2014; **46**(1):493-517.
20. Schmid PJ. Nonmodal stability theory. *Annual Review of Fluid Mechanics* 2007; **39**(1):129–162.
21. Chandler GJ, Juniper MP, Nichols JW, Schmid PJ. Adjoint algorithms for the Navier–Stokes equations in the low Mach number limit. *Journal of Computational Physics* 2012; **231**(4):1900–1916.

22. Marquet O, Sipp D, Jacquin L. Sensitivity analysis and passive control of cylinder flow. *Journal of Fluid Mechanics* 2008; **615**:221–252.
23. Meliga P, Sipp D, Chomaz MJ. Effect of compressibility on the global stability of axisymmetric wake flows. *Journal of Fluid Mechanics* 2010; **660**:499–526.
24. Meliga P, Pujals G, Serre É. Sensitivity of 2-D turbulent flow past a D-shaped cylinder using global stability. *Physics of Fluids* 2012; **24**(6):061701.
25. Mettot C, Renac F, Sipp D. Computation of eigenvalue sensitivity to base flow modifications in a discrete framework: application to open-loop control. *Journal of Computational Physics* 2014; **269**(0):234–258.
26. Mettot C, Sipp D, Bézard H. Quasi-laminar stability and sensitivity analyses for turbulent flows: prediction of low-frequency unsteadiness and passive control. *Physics of Fluids (1994-present)* 2014; **26**(4).
27. Fosas De Pando M, Sipp D, Schmid PJ. Efficient evaluation of the direct and adjoint linearized dynamics from compressible flow solvers. *Journal of Computational Physics* 2012; **231**(23):7739–7755.
28. Knoll DA, Keyes DE. Jacobian-free Newton–Krylov methods: a survey of approaches and applications. *Journal of Computational Physics* 2004; **193**(2):357–397.
29. Karniadakis GE, Sherwin S. *Spectral/hp Element Methods for Computational Fluid Dynamics*. Oxford Science Publications: Oxford, 2005.
30. Lyness JN. Numerical algorithms based on the theory of complex variable. *A.C.M. National Meeting*, New York, 1967; 125–133.
31. Lyness JN, Moler CB. Numerical differentiation of analytic functions. *SIAM Journal for Numerical Analysis* 1967; **4**(2):202–210.
32. Lai KL, Crassidis JL, Cheng Y, Jongrae K. New complex-step derivative approximations with application to second-order Kalman filtering. *AIAA-2005-5944*, University at Buffalo, State University of New York: Amherst, NY 14260–4400, 2005.
33. Kopriva DA. *Implementing Spectral Methods for Partial Differential Equations*. Springer, 2009.
34. Canuto C, Hussaini MY, Quarteroni A, Zang TA. *Spectral Methods in Fluid Dynamics*. Springer: New York, 1988.
35. Toro EF. *Riemann Solvers and Numerical Methods for Fluid Dynamics : A Practical Introduction*. Springer: Berlin, New York, 1997.
36. Arnold DN, Brezzi F, Cockburn B, Marini LD. Unified analysis of discontinuous Galerkin methods for elliptic problems. *SIAM Journal of Numerical Analysis* 2001; **39**(5):1749–1779.
37. (Available from: http://mumps.enseeiht.fr/) [accessed on 17 September 2014].
38. (Available from: http://www.netlib.org/lapack/) [accessed on 17 September 2014].
39. Martins JRRA, Sturdza P, Alonso JJ. The complex-step derivative approximation. *ACM Transactions on Mathematical Software* September 2003; **29**(3):245–262.
40. An H-B, Wen J, Feng T. On finite difference approximation of a matrix-vector product in the Jacobian-free Newton–Krylov method. *Journal of Computational and Applied Mathematics* 2011; **236**(6):1399–1409.
41. Ferrer E, deVicente J, Valero E. Low cost 3D global instability analysis and flow sensitivity based on dynamic mode decomposition and high order numerical tools. *International Journal for Numerical Methods in Fluids* 30 September 2014; **76**(3):169–184. To appear.
42. Meseguer-Garrido F, de Vicente J, Valero E, Theofilis V. On linear instability mechanisms in the incompressible open cavity flow. *Journal of Fluid Mechanics* 2014; **752**:219–23.
43. Rowley CW, Colonius T, Basu AJ. On self-sustained oscillations in two-dimensional compressible flow over rectangular cavities. *Journal of Fluid Mechanics* 2002; **455**:315–346.
44. Basley J, Pastur LR, Delprat N, Lusseyran F. Space-time aspects of a three-dimensional multi-modulated open cavity flow. *Physics of Fluids (1994-present)* 2013; **25**:064105.